# Transition from gravito- to electroconvective regimes in thin-layer electrodeposition

G. Gonzalez,[1,2] G. Marshall,[2] F. Molina,[1] and S. Dengra[2]
[1]*INQUIMAE, Facultad de Ciencias Exactas y Naturales, Universidad de Buenos Aires, 1428 Buenos Aires, Argentina*
[2]*Laboratorio de Sistemas Complejos, Facultad de Ciencias Exactas y Naturales, Universidad de Buenos Aires, 1428 Buenos Aires, Argentina*

(Received 13 January 2002; published 21 May 2002)

The transition from gravitoconvective to electroconvective prevailing regimes in thin-layer electrochemical deposition is analyzed through variations of electrolyte viscosity at constant cell thickness. The distribution of velocity directions at the deposit front is a measure of the relative weight of electroconvection versus gravitoconvection, and a signature of that transition. The experiments are carried out under galvanostatic conditions in convection prevailing regimes. Particle image velocimetry reveals that at low viscosities, buoyancy driven convection dominates; as viscosity increases, electrically driven convection becomes more important, eventually prevailing. The transition is observed at 1.5 times the viscosity of water. The theoretical model presented reveals that an increase of the Poisson and Reynolds numbers and a decrease of the Peclet and electric Grashof numbers, when viscosity increases, makes the electroconvective motion relatively more important. The model predicts a transition at approximately two times the viscosity of water. We may conclude that, in a physicochemical hydrodynamic flow involving ions, under galvanostatic conditions, increasing viscosity damps gravitoconvection and enhances electroconvection.

DOI: 10.1103/PhysRevE.65.051607 PACS number(s): 82.45.Qr, 47.20.Bp, 89.90.+n

## I. INTRODUCTION

In electrochemical thin-layer electrodeposition (ECD), the use of relatively high current densities, along with the absence of support electrolyte, give rise to complex, branched growth morphology [1]. In this situation, the transport of ions in the electrochemical cell is due to a combination of migration, diffusion, and convection. The relevance of convection, relative to migration and diffusion, in ion transport and growth morphology in ECD, for cells with thickness larger than 50 $\mu$m, has been demonstrated by a number of researchers [2–21]. In cells with thickness less than 50 $\mu$m, diffusion and migration are the dominant modes in ion transport as shown by Leger *et al.* [17]. Convection is driven mainly by Coulombic forces due to local charges [8,9,15], and by buoyancy forces due to concentration gradients that lead to density gradients [14,15]. When ramified deposits form, they interact with gravity driven vortex tubes and electric driven vortex rings, yielding a complex three-dimensional helicoidal fluid motion. The only way to assess quantitatively those interactions is through fluid velocity direction measurements. In this way, the relative weight of gravity to electroconvection can be determined. The study of the relative weight of electroconvection against gravitoconvection in ECD is relevant because it determines the flow regime and thus ion transport and growth morphology. One way to analyze this problem is through variations in cell thickness [15,22]; an alternative shown below, is through electrolyte viscosity variations. The former was addressed in the works of Huth *et al.* [15], and Marshall *et al.* [22]. In Ref. [22], a theoretical analysis was performed in which the equations describing ECD are written in terms of dimensionless quantities. In particular the gravity Grashof Gg and the electric Grashof Ge numbers represent the relative strength of the electric and gravity forces, respectively. The ratio $\lambda = \mathrm{Gg}/\mathrm{Ge}$ was introduced to express the importance of gravitoconvection as compared to electroconvection. It was found that the variations of $\lambda$ correlate well with the changes in the relative importance of both modes when the thickness was varied. Viscosity is a key parameter to analyze the influence of convection. In a typical hydrodynamic flow, increasing viscosity produces a general damping of the flow pattern. In a physicochemical hydrodynamic flow involving ions, the situation is more complex as shown below. In a recent paper, Gonzalez *et al.* [23] presented an extensive experimental and theoretical study of the role of viscosity in ECD under galvanostatic conditions, where viscosity was changed through glycerol additions. Experiments revealed that increasing viscosity, convection decreased and concentration gradients were more pronounced, while electric resistance and voltage increased. Concentration and convective fronts slowed down with viscosity, but their time scaling followed the same law as for solutions without glycerol, only differing by a constant. The theoretical model presented, based on that introduced by Marshall *et al.* [22], describes diffusive, migratory and convective ion transport in a fluid subject to an electric field. It is shown theoretically that, under galvanostatic conditions, while the gravity Grashof number remains constant, the electric Grashof number increases with viscosity. This fact demonstrates that electric forces increase relative to gravity ones as viscosity increases, thus motivating the present work. In this paper we study through experiments, theory and computational modeling, the relative importance of gravitoconvection vis-a-vis electroconvection in ECD. The transition from gravity to electroconvective prevailing regimes is analyzed through variations of electrolyte viscosity at constant cell thickness and under galvanostatic conditions. In particular we measure fluid velocities by means of particle image velocimetry (PIV) using micron sized particles. Viscosity variations are achieved by means of glycerol addition. The distribution of velocity directions at the deposit front is a measure of the relative

 

TABLE I. Definitions and values of experimental dimensionless numbers.

| Number | Definition | $\nu_0$ | $1.3\nu_0$ | $1.8\nu_0$ | $2.5\nu_0$ | $3.8\nu_0$ |
|---|---|---|---|---|---|---|
| Migration | $M_C=\mu_C\Phi_0/x_0u_0$ | 0.66 | 0.66 | 0.66 | 0.66 | 0.66 |
| | $M_A=\mu_A\Phi_0/x_0u_0$ | 1.0 | 1.0 | 1.0 | 1.0 | 1.0 |
| Peclet | $\mathrm{Pe}_C=x_0u_0/D_C$ | 18 | 23 | 31 | 44 | 66 |
| | $\mathrm{Pe}_A=x_0u_0/D_A$ | 12 | 15 | 21 | 29 | 43 |
| Poisson | $\mathrm{Po}=x_0^2C_0e/\epsilon\Phi_0$ | $18\times10^8$ | $15\times10^8$ | $11\times10^8$ | $8.9\times10^8$ | $6.5\times10^8$ |
| Reynolds | $\mathrm{Re}=x_0u_0/\nu$ | $12\times10^{-3}$ | $9.7\times10^{-3}$ | $7.3\times10^{-3}$ | $5.3\times10^{-3}$ | $3.7\times10^{-3}$ |
| Froude | $\mathrm{Fr}=u_0^2/x_0g$ | $1.3\times10^{-7}$ | $1.3\times10^{-7}$ | $1.3\times10^{-7}$ | $1.3\times10^{-7}$ | $1.3\times10^{-7}$ |
| Electric Grashof | $\mathrm{Ge}=eC_0\Phi_0/\rho_0u_0^2$ | $2.3\times10^{12}$ | $3.0\times10^{12}$ | $3.9\times10^{12}$ | $5.4\times10^{12}$ | $7.9\times10^{12}$ |
| Gravity Grashof | $\mathrm{Gg}_C=x_0C_0g\alpha_C/u_0^2$ | $4.7\times10^4$ | $4.7\times10^4$ | $4.7\times10^4$ | $4.7\times10^4$ | $4.7\times10^4$ |
| | $\mathrm{Gg}_A=x_0C_0g\alpha_A/u_0^2$ | $7.1\times10^4$ | $7.1\times10^4$ | $7.1\times10^4$ | $7.1\times10^4$ | $7.1\times10^4$ |

weight of electroconvection versus gravitoconvection, a signature of that transition. The remainder of the paper is organized as follows. In the following section we examine the theoretical model describing ECD. Experimental setup and results are presented in Secs. III and IV. Section V addresses the computational modeling results. The final section draws some general conclusions.

## II. THEORETICAL ANALYSIS

In a typical experiment, when the circuit is closed the current starts flowing through the electrolyte: cations and anions move towards the cathode and anode, respectively. Because of ion depletion near the cathode (cation aggregation and anion migration) and ion enhancement near the anode (anions piling up and cations entering through the dissolving anode), in an initial period—that is, before any growth is visible in the cathode—zones with low concentration near the cathode and high concentration near the anode develop rapidly. These are separated by an initial concentration value zone. Near the cathode the density is lower than the bulk electrolyte, while at the anode it is higher. This unstable configuration generates a density current flow at both electrodes: at the cathode the fluid ascends towards the top confining plate and at the anode descends towards the bottom. They generate two vortex tubes or rolls moving in opposite directions [14,15]. During this initial period cation depletion at the cathode is supposed to be uniform. Simultaneously, in a very narrow region near the cathode a local charge develops due to ionic depletion, giving rise to Coulombic forces initially pointing towards the cathode. After the initial period, which typically last few seconds, an instability develops by which the branched deposit growth is triggered. Imaging the deposit as a three-dimensional array of thin porous metallic filaments, Coulombic forces concentrate at their tips according to a model developed in Ref. [16]; each filament allows fluid to penetrate its tip and be ejected from the sides, configuring a toroidal vortex ring driven by the electric force. In the quasiplane of the growth, the previous three-dimensional picture reduces to the pair of counterrotating vortices and arcs at the tips of each filament as described by several authors [7–13,16]; in the plane normal to both, the quasiplane of the growth and the electrodes, it reduces to a pair of vortex rolls. The phenomenological model discussed above can be described using the Nernst-Planck equations for transport of ions [24–26], the Poisson equation for the electric potential, and the Navier-Stokes equations for the fluid flow. This model is an extension of the models introduced by Marshall *et al.* [22,27]. The dimensionless system of equations is

$$\frac{\partial C_i}{\partial t}=-\boldsymbol{\nabla}\cdot\mathbf{j}_i \tag{1}$$

$$\mathbf{j}_i=-M_iC_i\nabla\phi-\frac{1}{\mathrm{Pe}_i}\boldsymbol{\nabla}C_i+C_i\mathbf{v} \tag{2}$$

$$\boldsymbol{\nabla}^2\phi=\mathrm{Po}\sum_i z_iC_i \tag{3}$$

$$\frac{\partial\mathbf{v}}{\partial t}+\mathbf{v}\cdot\boldsymbol{\nabla}\mathbf{v}=-\boldsymbol{\nabla}P+\frac{1}{\mathrm{Re}}\boldsymbol{\nabla}^2\mathbf{v}+\left(\frac{1}{Fr}+\sum_i \mathrm{Gg}_i\Delta C_i\right)\frac{\mathbf{g}}{g}+\mathbf{E}\,\mathrm{Ge}\sum_i z_iC_i \tag{4}$$

$$\boldsymbol{\nabla}\cdot\mathbf{v}=0 \tag{5}$$

Here $C_i$ and $\mathbf{j}_i$ are the dimensionless concentration and flux of an ionic species $i$ (for a ternary electrolyte such as $ZnSO_4/H_2SO_4$, $i=C$, $A$, and $H$, standing for zinc, sulphate, and hydrogen ions); $\mathbf{v}$, $\phi$, $P$, and $\mathbf{E}$ are the dimensionless fluid velocity, electrostatic potential, pressure, and electric field, respectively; $\mathbf{g}/g$ is a unit vector pointing in the direction of gravity. The dimensionless numbers are defined in Table I (for details, see [23]). In Ref. [23] the quantities $z_i$, $\mu_i$, and $D_i$ are, respectively, the number of charges per ion, mobility, and diffusion constants of an ionic species $i$; $\mu_i$ and $z_i$ are signed quantities, being positive for cations and negative for anions; $g$ is the dimensional gravitational acceleration; $e$ is the electronic charge, $\epsilon$ is the permittivity of the medium and $\nu$ is the kinematic viscosity. $x_0$, $u_0$, $\Phi_0$, $C_0$, and $\rho_0$ are reference values of the length, velocity, electrostatic potential, concentration, and fluid density, respectively.

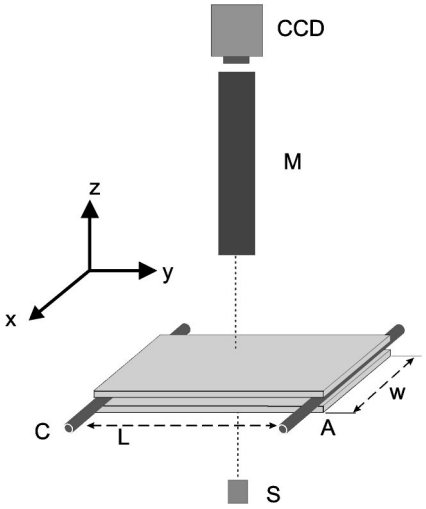


FIG. 1. Schematic diagram of the experimental system for particle tracking. *S*, light source; *M*, Navitar long working distance microscope; CCD, video camera.

For system closure, a Boussinesq-like approximation has been used for the fluid density: $\rho=\rho_o(1+\Sigma_i\alpha_i\Delta C_i)$, where $\alpha_i=1/\rho_o\partial\rho/\partial C_i$.

Numerical solutions to these equations are presented in the numerical simulation section.

### III. EXPERIMENTAL SETUP

Figure 1 shows a typical cell used in our ECD experiments. It consists of a thin layer of unsupported electrolyte confined between two parallel glass plates. The electrolyte solution was 0.1 M ZnSO4. To increase viscosity, solutions with glycerol additions between 0% and 40% in weight were employed. They correspond to increases in viscosity from 0 to 3.75 $\nu_0$, respectively, where $\nu_0$ is the viscosity of pure water. Zinc wire electrodes were placed at the two ends of the cell with a separation $L=15$ mm; their thickness (0.50 mm) defined the thickness $d$ of the cell. The cell width was $w=25$ mm. Experiments were performed under galvanostatic conditions.

The optical setup is similar to that described in Ref. [23]. The image is viewed with a charge-coupled device (CCD) video camera with a 50 mm $f/1.4$ camera lens. For fluid tracking, latex spheres of 0.9 $\mu$m diameter were added to the electrolyte as flow visualization particles. To observe them, a Navitar long working distance microscope (M) was used. Video images were digitized and saved to disk at up to 10 frames/s with a spatial resolution of up to 3 $\mu$m/pixel. A public domain software package [28], was used for image capturing and processing. Image processing techniques where employed to enhance particle detection. A PIV algorithm was employed for trajectories detection and velocity computations.

### IV. EXPERIMENTAL RESULTS

In the following set of experiments we show the influence of viscosity on the deposit morphology and convection regime. These experiments are governed by a set of dimensionless numbers presented in Table I. They show that increasing viscosity under galvanostatic conditions decreases the ratio λ. Figure 2 shows the evolution of the deposit growth, for the first 30 s, in a cell with $d=0.50$ mm under galvanostatic conditions ($I=10$ mA) when viscosity is increased. The rows correspond to different values of glycerol concentration. From top to bottom: 0%, 10%, 20%, 30%, and 40%, respectively. Each column shows snapshots at different times

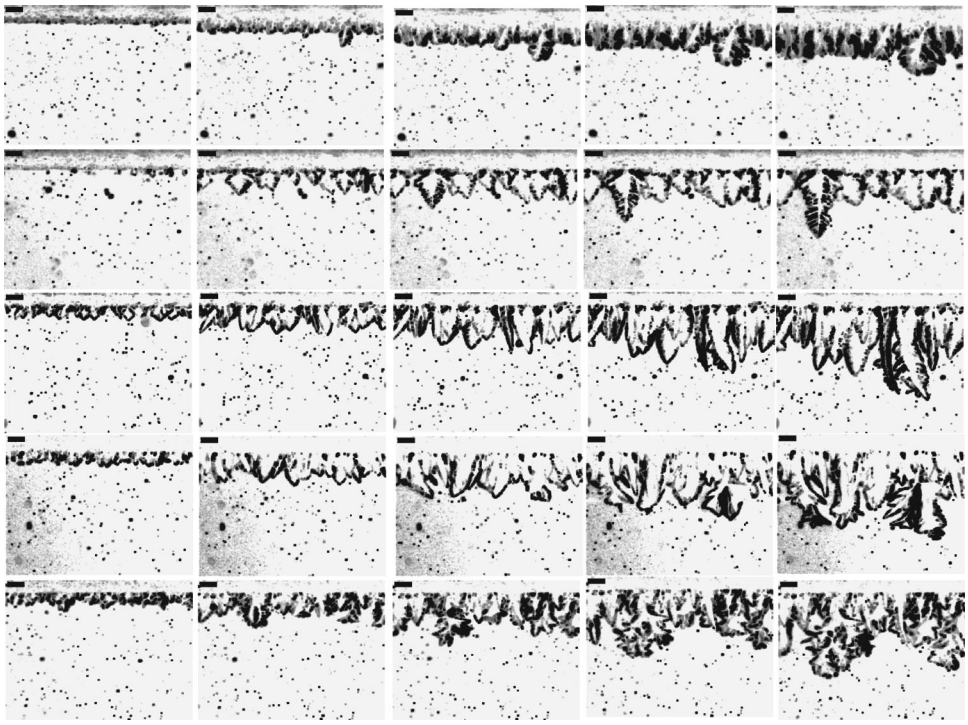

FIG. 2. Snapshots of the deposit growth for different viscosities (0.50 mm and 10 mA). Each column corresponds to a different time; from left to right: t = 0, 6, 12, 18 and 24 s. In each column, each frame corresponds to different glycerol concentrations; from top to bottom: 0%, 10%, 20%, 30% and 40%, respectively. Frame dimensions: 1.53 mm wide and 1.17 mm in height.

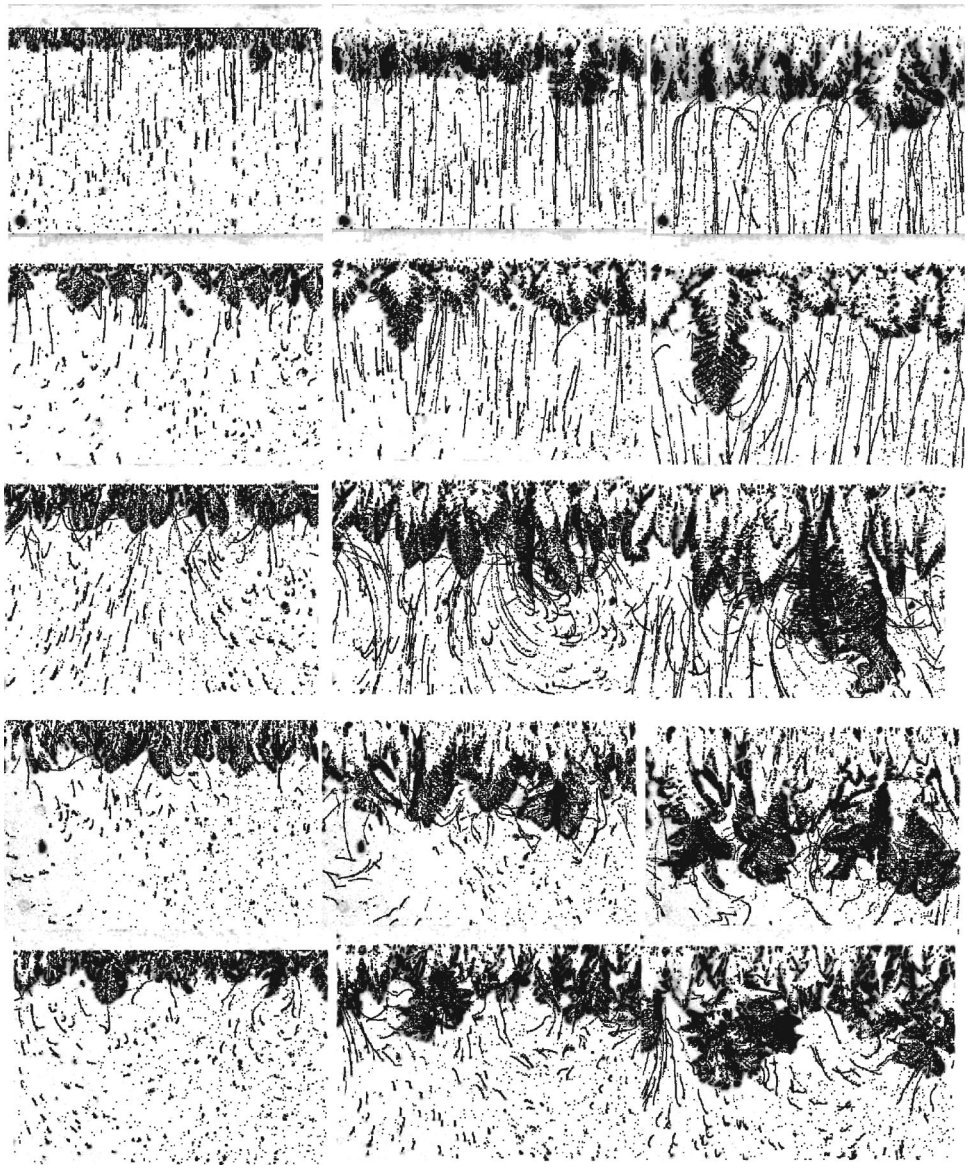

FIG. 3. Top view cell visualization of 1 $\mu$m sized particle trajectories near the deposit front. To show the motion of tracer particles, in each frame, several digital images (spanning an interval of 10 s) were superimposed and thresholded. From left to right, each column represents a different time interval: left, 0–10 s; center, 10–20 s; right, 20–30 s. From top down, each row corresponds to a different value of glycerol concentration: 0%, 10%, 20%, 30%, and 40%, respectively. Frame dimensions: 1.53 mm wide and 1.17 mm in height.

(time increasing from left to right). At the scales shown in the pictures (time scale: the first 30 s, spatial scale 1 mm), the deposit varies from compact to dendritic, as viscosity increases. This variation is reversed at longer times and larger spatial scales (as observed in Ref. [23]), in which few branches survive at low viscosities, while a more compact structure emerges at higher viscosities. Now we analyze the pattern of convective motion by particle tracking. Figure 3 shows a top view of the cell, near the deposit front, visualizing the fluid flow through particle trajectories. Here, the cell was 0.50 mm thick, 25 mm wide and subject to a constant current $I=10$ mA. Several digital images spanning an interval of 10 s (left column, 0-10 s; center column, 10–20 s; right column, 20–30 s) are superimposed and thresholded to show the motion of the tracer particles. From top down in each column, each frame represents a different value of glycerol concentration: 0%, 10%, 20%, 30%, and 40$w/w$, respectively, yielding viscosities from $\mu_0$ to 3.8 $\mu_0$, respectively, where $\mu_0$ is the water viscosity. In almost all the frames, two regions are observed: (a) a zone with a convection dominated flow, with long, continuous trajectories; and (b) a steady state region in which a Brownian motion is observed, with very short trajectories. In the convection dominated zone, we can distinguish gravity driven convection dominated flow (particle trajectories, entrained in a vortex tube with an horizontal axis, are projected as lines in the plane of the cell, moving upwards near the deposit front and downwards in the zone limit) and electroconvection dominated flow (particle trajectories entrained in a toroidal vortex ring centered at a tip branch are projected as a circle in the plane of the cell). In the top two rows, gravitoconvection prevails as revealed by the linear trajectories, while in the remaining rows, due to an increase in viscosity, the gravitoconvection is attenuated and electroconvection prevails as shown by the near circular trajectories. In the bottom frames the increase of viscosity produces a substantial damping of convection. It is also observed that convection takes longer time to establish itself in electroconvective regimes than in gravitoconvective ones (compare, for instance, first and last rows of Fig. 3). The relative importance of gravitoconvection and electroconvec-

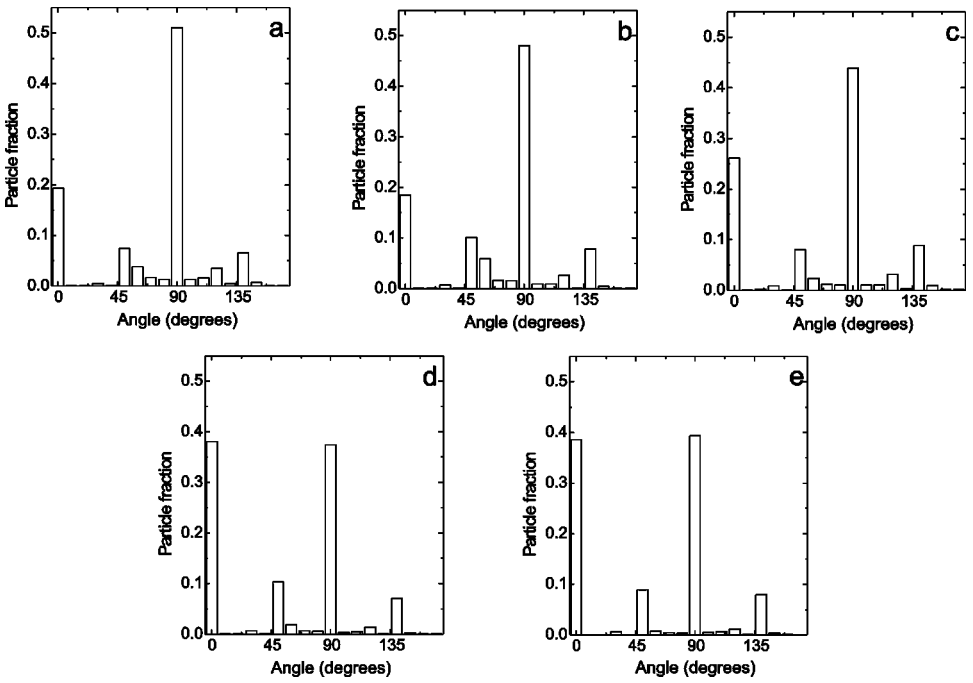


FIG. 4. Distribution of particle velocity vector directions (in the 10–20 s interval) for different angles, where a 0 ° angle means motion parallel to the cathode. Each graph corresponds to a different value of glycerol concentration: (a) 0%, (b) 10%, (c) 20%, (d) 30%, and (e) 40%, respectively.

tion can be assessed measuring the velocity direction: in pure gravitoconvection regimes a top view of the cell will show the projection of the vortex tube trajectories as lines normal to the cathode, while in pure electroconvection regimes a top view will show circular trajectories. Thus, Fig. 4 shows the distribution of particle directions (in the 10–20 s interval) obtained by the tracking algorithm, for different angles. Here, a 0 ° angle means motion parallel to the cathode. It is seen in Fig. 4(a) that for 0% glycerol the dominant direction is perpendicular to the electrode, indicating a gravitoconvective dominant regime. As viscosity is increased, Fig. 4(e) for 40% glycerol the parallel and normal direction have similar weight, revealing a circular motion, and thus electroconvective prevailing conditions.

Considering the values of velocity, Fig. 5 shows averages of the normal ($\langle \nu_\perp \rangle$) and parallel ($\langle \nu_\parallel \rangle$) velocity components, and of the absolute value of velocity ($\langle \nu \rangle$), as a function of viscosity. We observe a decrease in the absolute value as expected. The normal component decreases as viscosity increases, while the parallel one remains approximately constant. This corresponds to a decrease of gravitoconvection relative to electroconvection (this is further elaborated in Fig. 6, below). To estimate the average gravitoconvective ($\langle \nu_G \rangle$) and electroconvective ($\langle \nu_E \rangle$) vortex speeds, we assume that the normal and parallel components, measured from their projection on the cell plane, are related to the former by $\langle \nu_\parallel \rangle = \langle \nu_E \rangle$, and $\langle \nu_\perp \rangle = \langle \nu_G \rangle + \langle \nu_E \rangle$. This is based upon the fact that, since we are measuring on a projection on the plane of the cell, the electroconvective motion is seen as a circular motion ($\langle \nu_{E,\perp} \rangle = \langle \nu_{E,\parallel} \rangle$) whereas the gravitoconvective motion is seen as a line ($\langle \nu_{G,\parallel} \rangle = 0$). Figure 6 shows the results for $\langle \nu_E \rangle$ and $\langle \nu_G \rangle$ as a function of viscosity. We observe a crossover at about $1.5\nu_0$ corresponding to a transition between gravitoconvection and electroconvection. It is observed that $\langle \nu_E \rangle$ in Fig. 6 appears to be approximately independent of viscosity, whereas in Fig. 3, for 0% glycerol, there are almost no circular trajectories visible. This effect is due to the inability of the tracking algorithm to cope with the three-dimensional (3D) nature of particles motion and field depth effects. In fact, theoretical considerations predict that electroconvective motion should increase with viscosity due to the voltage increase as viscosity increases.

## V. NUMERICAL SIMULATIONS

The three-dimensional model presented in Sec. II is treated as a set of two bidimensional models in a horizontal and a vertical plane, respectively, [22,27]. The horizontal plane model constitutes what we call the top view model while the vertical plane model constitutes the side view model. The top view model is invariant under gravity forces (gravity is normal to the plane of the cell). In the side view model, electric and gravity forces are coplanar. The computational model solves the previous systems, for each time step, in a fixed domain, in a 2D uniform lattice (equal spac-

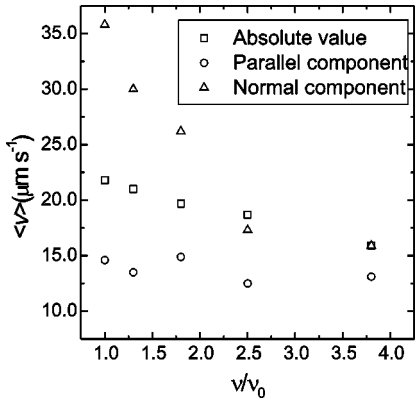


FIG. 5. Average velocities: Absolute value, parallel and normal components (referred to the cathode), as a function of viscosity.

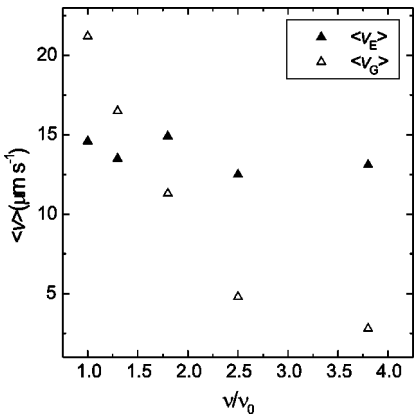


FIG. 6. Average values of the experimental electroconvective and gravitoconvective velocities as a function of viscosity.

ing in both directions) using finite differences and deterministic relaxation techniques (details can be found in [22] and [27]. The interface is moved at random using a dielectrical breakdown model [29].

In the following we present numerical results obtained with the side and top view models in the simulation of ECD experiments (a growthless process is asumed) in which the relative importance of gravitoconvection as compared to electroconvection is analyzed, through viscosity variations. This pretends to mimic the physical experiments presented in the preceding section. The simulations are described by the set of dimensionless numbers shown in Table II. (The Froude number is not present in the transport-vorticity form of the equations used in the simulations). The values of the Poisson and electric Grashof numbers differ from typical experiments (compare Tables II and I). This is due to numerical limitations: higher values of those numbers imply steeper gradients in the solution, thus requiring finer grids and consequently, large computational facilities. The computational model is written in the *C* language and implemented on a Pentium class computer under Linux. The side view model uses a rectangular cell of $800\times25$ nodes for different values of the dimensionless numbers, while the top view model uses a rectangular cell of $400\times200$ nodes for the same set of the dimensionless numbers.

Figures 7 and 8 present top and side view model results, respectively, in an earlier stage of the simulation for different

TABLE II. Values of the numerical dimensionless numbers.

| Symbol | $\nu_0$ | $1.3\nu_0$ | $1.8\nu_0$ | $2.5\nu_0$ | $3.8\nu_0$ |
|---|---|---|---|---|---|
| $M_C$ | 0.66 | 0.66 | 0.66 | 0.66 | 0.66 |
| $M_A$ | 1.0 | 1.0 | 1.0 | 1.0 | 1.0 |
| $\mathrm{Pe}_C$ | 18 | 23 | 31 | 44 | 66 |
| $\mathrm{Pe}_A$ | 12 | 15 | 21 | 29 | 44 |
| Po | $5.0\times10^{2}$ | $4.7\times10^{2}$ | $3.7\times10^{2}$ | $2.9\times10^{2}$ | $2.0\times10^{2}$ |
| Re | $12\times10^{-3}$ | $9.7\times10^{-3}$ | $7.4\times10^{-3}$ | $5.3\times10^{-3}$ | $3.7\times10^{-3}$ |
| Ge | $1.0\times10^{4}$ | $1.6\times10^{4}$ | $2.2\times10^{4}$ | $2.9\times10^{4}$ | $3.4\times10^{4}$ |
| $\mathrm{Gg}_C$ | $1.0\times10^{4}$ | $1.0\times10^{4}$ | $1.0\times10^{4}$ | $1.0\times10^{4}$ | $1.0\times10^{4}$ |
| $\mathrm{Gg}_A$ | $1.0\times10^{4}$ | $1.0\times10^{4}$ | $1.0\times10^{4}$ | $1.0\times10^{4}$ | $1.0\times10^{4}$ |

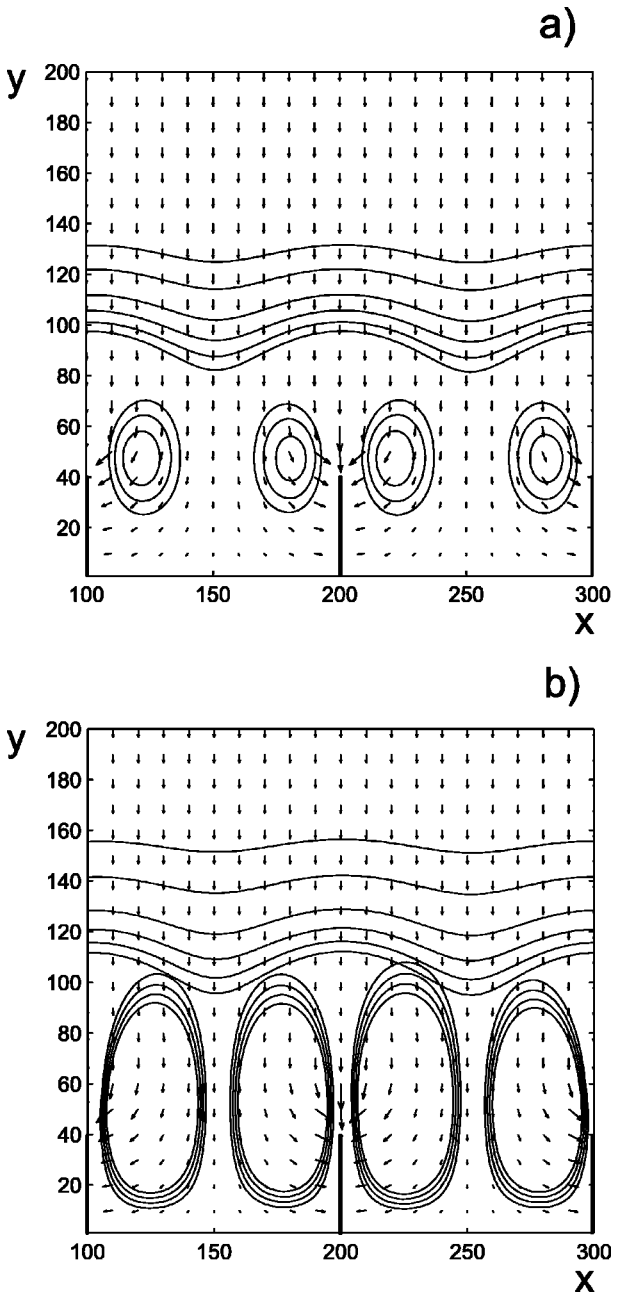


FIG. 7. Top view simulations (in a region near the cathode), for an earlier stage of the simulation, for: (a) 0% and (b) 40% glycerol. Superimposed contour lines of the stream function and cation concentration and the electric vector field are shown.

values of viscosity, and for an enlarged region near the cathode. They show superimposed, stream function and cation concentration contour lines, and the electric field. Also shown in Fig. 7 are the spikes introduced to simulate the deposit growth. These pictures show vividly the existence of electric dipoles, concentration fronts and vortex rolls. In Fig. 7 the electric vector field reveals its convergence to the deposit tips. Here the motion is restricted to the zone near the cathode. Figure 9 shows, in circles, the average gravitoconvective velocity and, in squares, the electroconvective vortex velocity, as a function of viscosity under galvanostatic conditions. For averaging velocities, we used the region near the

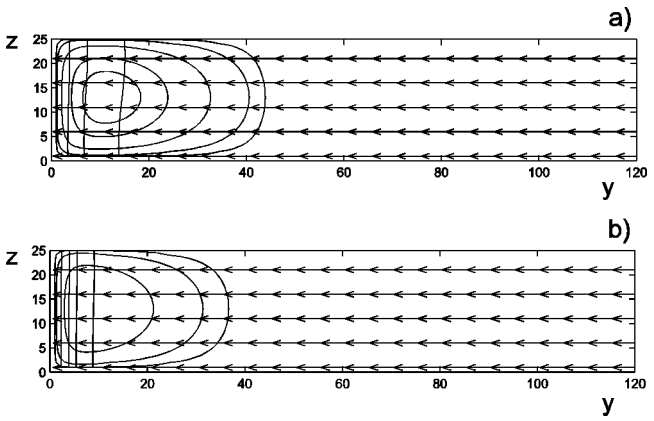


FIG. 8. Side view simulations (in a region near the cathode), for an earlier stage of the simulation, for: (a) 0% and (b) 40% glycerol. Superimposed contour lines of the stream function and cation concentration are shown.

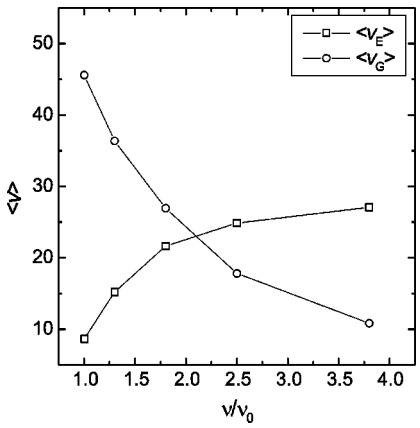


FIG. 9. Dimensionless average values of the simulated electroconvective (squares) and gravitoconvective (circles) velocities as a function of viscosity.

cathode or the deposit front, where motion is observed. The averaged gravitoconvective velocity decreases with viscosity as expected, similar to what happens with the $\langle \nu_G \rangle$ values obtained from experiments. The averaged electroconvective velocity increases, because an increase in viscosity under galvanostatic conditions, produces an increase in voltage. This is in qualitative agreement with the results of Fig. 3. The experimental electroconvective velocity (Fig. 6) appears to be constant, due to the algorithm shortcomings already mentioned. In summary, the numerical results show that when viscosity increases, velocities in the top view model are larger than those in the side view model. Contrarily, when viscosity decreases, velocities in the side view model are larger than in the top view model.

## VI. DISCUSSION

The observable for analyzing the transition from gravity to electroconvective prevailing regimes in ECD is the distribution of fluid velocity directions near the deposit front. Its measurement shows that by increasing the viscosity the intensity of gravitoconvective motion decreases, while electroconvective motion becomes relatively stronger. Under galvanostatic conditions, as viscosity increases, the electric field and the electric forces increase, yielding the observed increase of electroconvection with viscosity. A transition from gravitoconvective to electroconvective regime is observed at about $\nu = 1.5\nu_0$. Our theoretical model predicts, through the analysis of the dimensionless numbers (see Table I), that increasing viscosity diffusion and convection slow down, as shown by the variations of Pe and Re. Migration is invariant in the present conditions ($M$ values are constant), because the electric field is increased to keep the current constant. This electric field increase yields larger Ge values (higher electric forces), too. On the other hand, the Gg are constant, due to the fact that constant current yields equal density gradients and thus constant buoyant forces. Therefore, increasing viscosity under galvanostatic conditions decreases the ratio λ. Our two-dimensional numerical models (top and side view models) are used to analyze the experimental behavior. In these models, as in the experiments, we compute average velocities to study the transition from gravitoconvective to electroconvective regimes (through viscosity variations). These results are depicted in Figs. 7 and 8. Their analysis show the same trends as in the experiments: electroconvective vortices in Fig. 7(b) are larger than those of Fig. 7(a), due to the electric field increase caused by higher viscosity. The figure shows arcs of concentration contour lines, surrounding each tip, containing the vortex dipole associated with that tip, and two limiting zones: an inner zone almost depleted of ions, and an outer zone that rapidly reaches the bulk concentration value. This has been experimentally observed by many authors ( [11–13,16,19,21,30]). In Fig. 8, the slowing down of convective motion due to viscosity increase is clearly seen. Also, at a higher viscosity [Fig. 8(b)] the concentration gradients are steeper due to a decrease in diffusion. These predictions are confirmed by present and previous experimental results [23]. In summary, the simulations show that when viscosity increases, velocities in the top view model are larger than those in the side view model; when viscosity decreases, the situation is reversed. This is condensed in Fig. 9, where a transition is found at about $\nu = 2\nu_0$ , in a remarkable agreement with the experiments, which revealed a transition near $1.5\nu_0$. Concluding, our velocity measurements allow a quantitative assessment of the viscosity influence over convective motion. It is found that in a physicochemical hydrodynamic flow involving ions, under galvanostatic conditions, increasing viscosity damps gravitoconvection and enhances electroconvection through electric field increase. These experimental results are interpreted in terms of the top view and side view theoretical-computational models. These models simulate the limiting cases of electrical driven or gravity driven convection prevailing regimes, respectively, as follows. The top view model describes adequately the experiments for high glycerol contents (high viscosity), an electroconvective prevailing regime, while the side view model describes the 0% glycerol experiments, a gravitoconvective regime. Thus, our theoretical-computational model is able to predict the main features of electrohydrodynamic flows, including the transition from gravitoconvective to electroconvective regimes.

**ACKNOWLEDGMENTS**

G.M. is thankful to the Fulbright Commission for financial support. G.M. and F.V.M. are investigators of the CONICET, Argentina. G.G. and S.D. are supported by CONICET and University of Buenos Aires, respectively. This work was partially supported by UBA Grant No. TX09/99, FOMEC Grant No. 376/98 from the Department of Computer Sciences, FCEyN, UBA and CONICET Grant No. PIP379/98.

[1] Y. Sawada, A. Dougherty, and J. P. Gollub, Phys. Rev. Lett. **56**, 1260 (1986); D. Grier, E. Ben-Jacob, R. Clarke, and L. M. Sander, *ibid.* **56**, 1264 (1986); T. Vicsek, *Fractal Growth Phenomena* (World Scientific, Singapore, 1992).

[2] R. M. Brady and R. Ball, Nature (London) **309**, 225 (1984).

[3] D. Barkey, J. Electrochem. Soc. **138**, 2912 (1991).

[4] F. R. McLarnon, R. H. Muller, and C. W. Tobias, Electrochim. Acta **21**, 101 (1976); Y. Fukunaka, T. Yamamoto, and Y. Kondo, J. Electrochem. Soc. **136**, 3630 (1989).

[5] R. H. Cork, D. C. Pritchard, and W. Y. Tam, Phys. Rev. A **44**, 6940 (1991).

[6] P. Carro, S. L. Marchiano, A. Hernandez Creus, S. Gonzalez, R. C. Salvarezza, and A. J. Arvia, Phys. Rev. E **48**, 2374 (1993); P. Trigueros, J. Claret, F. Mas, and F. Sagues, J. Electroanal. Chem. Interfacial Electrochem. **312**, 219 (1991).

[7] V. Fleury, M. Rosso, J-N. Chazalviel, and B. Sapoval, Phys. Rev. A **44**, 6693 (1991).

[8] V. Fleury, J-N. Chazalviel, and M. Rosso, Phys. Rev. Lett. **68**, 2492 (1992).

[9] V. Fleury, J-N. Chazalviel, and M. Rosso, Phys. Rev. E **48**, 1279 (1993).

[10] C. Livermore and Po-zen Wong, Phys. Rev. Lett. **72**, 3847 (1994).

[11] V. Fleury, J. Kaufman, and B. Hibbert, Phys. Rev. E **48**, 3831 (1993).

[12] V. Fleury, J. Kaufman, and B. Hibbert, Nature (London) **367**, 435 (1994).

[13] M. Rosso, J-N. Chazalviel, V. Fleury, and E. Chassaing, Electrochim. Acta **39**, 507 (1994).

[14] D. P. Barkey, D. Watt, Z. Liu, and S. Raber, J. Electrochem. Soc. **141**, 1206 (1994).

[15] J. Huth, H. Swinney, W. McCormick, A. Kuhn, and F. Argoul, Phys. Rev. E **51**, 3444 (1995).

[16] V. Fleury, M. Rosso, and J-N. Chazalviel in *Fractal Aspects of Materials*, edited by Fereydoon Family*et al.* Mater. Res. Soc. Symp. Proc. **367** (Materials Research Society, Pittsburg, PA, 1995), p. 183.

[17] C. Leger, J. Elezgaray, and F. Argoul, Phys. Rev. Lett. **78**, 5010 (1997).

[18] K. A. Linehan and J. R. de Bruyn, Can. J. Phys. **73**, 177 (1995).

[19] J-N. Chazalviel, M. Rosso, E. Chassaing, and V. Fleury, J. Electroanal. Chem. **407**, 61 (1996).

[20] F. Argoul, E. Freysz, A. Kuhn, C. Leger, and L. Potin, Phys. Rev. E **53**, 1777 (1996).

[21] S. Dengra, G. Marshall, and F. Molina, J. Phys. Soc. Jpn. **69**, 963 (2000); G. Marshall, P. Mocskos, F. Molina, and S. Dengra, in *Electrochemical Synthesis and Modification of Materials*, edited by P. C. Corcovan *et al.*, Mater. Res. Soc. Symp. Proc. **451** (Materials Research Society, Pittsburg, PA, 1997), p. 147.

[22] G. Marshall, P. Mocskos, H. L. Swinney, and J. M. Huth, Phys. Rev. E **59**, 2157 (1999).

[23] G. Gonzalez, G. Marshall, F. V. Molina, S. Dengra, and M. Rosso, J. Electrochem. Soc. **148**, C479 (2001).

[24] A. J. Bard and L. R. Faulkner, *Electrochemical Methods, Fundamentals and Applications* (Wiley, New York, 1980).

[25] J. S. Newman, *Electrochemical Systems* (Prentice Hall, New Jersey, 1973).

[26] V. G. Levich, *Physicochemical Hydrodynamics* (Prentice Hall, New Jersey, 1962).

[27] G. Marshall and P. Mocskos, Phys. Rev. E **55**, 549 (1997); G. Marshall, E. Perone, P. Tarela, and P. Mocskos, Chaos, Solitons and Fractals **6**, 315 (1995); G. Marshall, P. Mocskos, and M. Olivella, in *Disordered Materials and Interfaces*, edited by H. E. Stanley *et al.*, Mater. Res. Soc. Symp. Proc. **407** (Materials Research Society, Pittsburg, PA, 1996), p. 355.

[28] NIH Image, available from http://rsb.info.nih.gov/nih-image/download.html

[29] L. Pietronero and H. J. Weismann, J. Stat. Phys. **36**, 909 (1984).

[30] V. Fleury, M. Rosso, and J-N. Chazalviel, Phys. Rev. A **43**, 6908 (1991).